RSC Advances

PAPER

View Article Online
View Journal | View Issue

Cite this: *RSC Adv.*, 2015, **5**, 68151

Controllable *in situ* synthesis of $BiOBr_xI_{1-x}$ solid solution on reduced graphene oxide with enhanced visible light photocatalytic performance†

Zhichong Yang,‡[a] Fuxing Cheng,‡[a] Xiaoping Dong*[a] and Fangming Cui*[b]

Received 7th May 2015
Accepted 30th July 2015

DOI: 10.1039/c5ra08416d

www.rsc.org/advances

Novel composite photocatalysts, $BiOBr_xI_{1-x}$–rGO, were facilely prepared by *in situ* controllable deposition of $BiOBr_xI_{1-x}$ solid solutions onto the surface of graphene oxide which was then reduced at mild conditions. The high-resolution transmission electron microscopy results revealed an intimate interface between $BiOBr_xI_{1-x}$ and rGO in the composites. The UV-vis diffuse reflectance spectra showed that $BiOBr_xI_{1-x}$–rGO composites had intense optical absorption in the visible light region. These excellent structural and spectral properties endowed $BiOBr_xI_{1-x}$–rGO composites with enhanced photocatalytic performance. Significantly, the $BiOBr_{0.6}I_{0.4}$–rGO sample exhibited the best photocatalytic activity for the photodegradation of methyl orange under visible light irradiation (λ > 420 nm). The enhanced photocatalytic activity could be attributed to more effective charge separation and transportation, and increased light absorption. The radical trapping experiments confirmed that holes and superoxide radical species were the two main reactive species in the photocatalysis process. Moreover, this material exhibited great stability and durability, which retained more than 80% degradation after several cycles.

Introduction

In the past two decades, semiconductor-based photocatalysis has received increasing attention because of its wide applications in energy generation and environmental purification.[1–3] However, traditional photocatalysts, such as TiO_2, ZnO_2, SnO_2 *et al.*, are faced with the low efficient utilization of natural sunlight and the high recombination of photogenerated carriers. Numerous semiconductors with narrow band gap have recently been studied as visible light harvesting photocatalysts. Among them, bismuth oxyhalides (BiOX, X = F, Cl, Br, I) have been extensively investigated owing to their unique layered structure and high stability.[4–8] All of the BiOX crystallize in the tetragonal matlockite structure comprising of $[Bi_2O_2]^{2+}$ slabs interleaved by double slabs of halogen atoms. The formed internal static electric fields between the negative halogen layers and the positive $[Bi_2O_2]^{2+}$ layer can efficiently promote the separation of photogenerated electron–hole pairs.[9–11]

However, the photocatalytic efficiency of pure BiOX is far from efficient for practical applications under visible light. Up to date, some strategies have been carried out, which includes the controlling synthesis of BiOX with specific morphology and structure,[12–16] constructing BiOX-based composites with other semiconductors (such as TiO_2,[17] ZnO,[18] C_3N_4,[19–21] AgX,[22] MoS_2,[23] Ag_3PO_4,[24] Bi_2S_3,[25] Bi_2WO_6,[26] $ZnFe_2O_4$ [27]) and doping with metal atoms[28–32] (such as Ag, Al, Fe, Ti, Mn). Besides, some BiOX–BiOY (X, Y = Cl, Br, I) composite systems have also been synthesized very recently, and all the alloyed compounds have been found to be more active than the pure phase.[33–36] The enhanced photocatalytic activity is mainly attributed to the intimately contacted interfaces in composites and well-aligned straddling band-structure that is favourable for the efficient transfer of photogenerated charges.

Graphene, a single layer of sp^2-bonded carbon atoms tightly packed into a two-dimensional honeycomb structure, has attracted great attention in electronic, optical and catalytic fields because of its outstanding mechanical, optical and electrical properties.[37–42] Due to the excellent mobility of charge carriers and extremely high theoretical specific surface area, graphene recently exhibited potential applications in photocatalysis including hydrogen production from photocatalytic water-splitting and photo-degradation of organic pollutants. As the electron acceptor, photogenerated electrons on conduction band are rapidly transported to graphene, and then reduce H_2O to produce H_2 or react with O_2 to form superoxide radicals ($^{\bullet}O_2^-$) with strongly oxidizing property. It has been reported that graphene (or reduced graphene oxides, rGO) based composite photocatalysts, such as graphene/BiOBr,[43] graphene/BiOI,[44] graphene/$BiOBr_{0.8}I_{0.2}$ [45] and graphene/BiOCl,[46] exhibited

[a]*Department of Chemistry, School of Sciences, Zhejiang Sci-Tech University, 928 Second Avenue, Xiasha Higher Education Zone, Hangzhou, 310018, China. E-mail: xpdong@zstu.edu.cn; Fax: +86 571 86843653; Tel: +86 571 86843228*

[b]*Qian Xuesen Laboratory of Space Technology, 104 Youyi Road, Haidian District, Beijing, China. E-mail: fmcui01@163.com; Fax: +86-10-68747505; Tel: +86-10-68113055*

† Electronic supplementary information (ESI) available. See DOI: 10.1039/c5ra08416d

‡ These authors contributed equally to this work.

enhanced photocatalytic performance in comparison with their corresponding individual semiconductor photocatalysts.

Herein, photocatalysts composing solid solution of bismuth oxyhalides ($BiOBr_xI_{1-x}$) and rGO, denoted as $BiOBr_xI_{1-x}$–rGO, were prepared by an *in situ* growth strategy of $BiOBr_xI_{1-x}$ on GO, followed by a reduction treatment. The phase composition, morphologies, microstructure and optical properties of these obtained photocatalysts were well characterized, and the influence of molar ratio of Br^-/I^- in solid solution on photocatalytic activity were also investigated. As an optimal sample, the $BiOBr_{0.6}I_{0.4}$–rGO composite showed excellent high photocatalytic activity in degradation of Methyl Orange (MO) under visible light ($\lambda > 420$ nm) irradiation. Furthermore, the possible mechanism for visible light driven photocatalytic reaction was also proposed.

Experimental

Synthesis of GO

Graphene oxide (GO) was prepared according to the modified Staudenmaier method.[43] In detail, 10 mL of HNO_3 (70%) and 18 mL of H_2SO_4 (98%) were mixed and stirred for 15 min in a 500 mL reaction flask immersed in an ice bath. Then amount of graphite (1 g) was added into the above concentrated acid mixture and stirred for 20 min. After that, the ice bath was removed, and 22 g of $KClO_3$ was added slowly into the solution. The reaction mixture was stirred continuously for 48 h at room temperature. Then, the mixture was added to excess distilled water, washed with 5% HCl solution, and then repeatedly washed with distilled water until the pH of the filtrate was ~7. To remove unexfoliated GO, the prepared GO was dispersed in distilled water with a concentration of 1 g L^{-1} and sonicated for 1 h. The dispersion was then centrifuged at 5000 rpm for 10 min, and the resultant homogeneous yellow-brown dispersion was then filtered through a 200 nm pore size polytetrafluoroethylene (PTFE) membrane. The exfoliated GO in the filtrates was then collected and dried in a vacuum oven at 40 °C overnight to get sample in powder form for further use.

Synthesis of $BiOBr_xI_{1-x}$–rGO composites

The $BiOBr_xI_{1-x}$–rGO composites were prepared *via* an *in situ* precipitation method. Firstly, measured amounts of KI and KBr were added into 100 mL 0.05 mg mL^{-1} GO suspension, and then the mixture was ultrasonicated for 30 min to obtain a uniform suspension. Meanwhile, a stoichiometric amount of $Bi(NO_3)_3 \cdot 5H_2O$ solid was dissolved in 1 mL glacial acetic acid to obtain a clear solution. Following, the solution was added rapidly to the suspension and subsequently stirred for 1 h at 65 °C. After adding a certain amount of ammonia and hydrazine monohydrate solution, the suspension was stirred at 65 °C for another 3.5 h. Finally, the obtained precipitation was filtrated, washed several times with deionized water and dried in a vacuum oven at 60 °C overnight.

Characterization

The crystal structure of samples was analyzed by an X-ray diffraction (XRD, DX-2700 diffractometer, Dandong Haoyuan Instrument Co. Ltd, China) with high-intensity Cu-Kα radiation ($\lambda = 0.15418$ nm). The step scan covered the angular range 5–70° in steps of 0.03°. The morphology and structure of samples were examined by a field emission scanning electron microscopy (FE-SEM, Hitachi S-4800) and transmission electron microscopy (TEM: JEOL-2100 electron microscope, Japan) at 200 kV. Raman spectra were recorded on a microscopic confocal Raman spectrometer with an excitation of 514.5 nm laser light at room temperature. UV-vis diffuse reflectance spectroscopy measurements were carried out using a Shimadzu UV-2450 spectrophotometer in the range of 200 to 800 nm with an integrating sphere using $BaSO_4$ as a reflectance standard material. The COD of photocatalytic solution was determined by a HACH DR1010 (USA) direct reading spectrophotometer using a HACH COD reactor.

Photocatalytic studies

The photocatalytic performance of as-prepared samples was evaluated by photodegradation of MO in aqueous solution under visible light irradiation. All the photocatalytic tests were carried out in a photochemical reactor (HSX-F300, Beijing NBet) equipped with a 300 W xenon lamp linking a 420 nm cut-off filter as light source. In each experiment, 100 mg of photocatalyst powder was added into 100 mL of MO solution with an initial concentration of 10 mg L^{-1}. Prior to illumination, the suspension was stirred in dark for 60 min to insure adsorption–desorption equilibrium of MO on photocatalyst surface. During the course of irradiation, 3.0 mL of suspension was withdrawn periodically from the reactor, followed by centrifugation and separation to remove the bottom photocatalyst particles. Finally, the supernatant liquid was measured on the Shimadzu UV-2450 spectrophotometer, and the degradation ratio of MO was obtained by calculating the concentration change (C/C_0) from the variation of absorbance (A/A_0) at 464 nm. C_0 and A_0 denote the concentration and absorbance of MO solution at the adsorption–desorption equilibrium.

Results and discussion

Characterization of $BiOBr_xI_{1-x}$–rGO composites

Fig. 1 exhibited XRD patterns of $BiOBr_xI_{1-x}$–rGO samples, as well as pure BiOBr and BiOI. It was found in Fig. 1a that all the diffraction peaks of pure BrOBr and BiOI could be respectively indexed to the tetragonal BiOBr phase (JCDPS 73-2061; $a = b =$ 3.915 Å, $c = 8.076$ Å) and the tetragonal BiOI phase (JCDPS 73-2062; $a = b = 3.984$ Å, $c = 9.128$ Å). After combining with rGO, the relative intensity of diffractions for BiOBr–rGO and BiOI–rGO obviously changed. The weakening and broadening of (001) diffractions revealed the decrease of BiOX thickness in *c* direction, which suggested the significant influence of rGO on the growth of BiOX. Because of the similar crystal structure and different halogen ion radius, BiOI possesses a relative large interlayer spacing in comparison with BiOBr. It was obvious

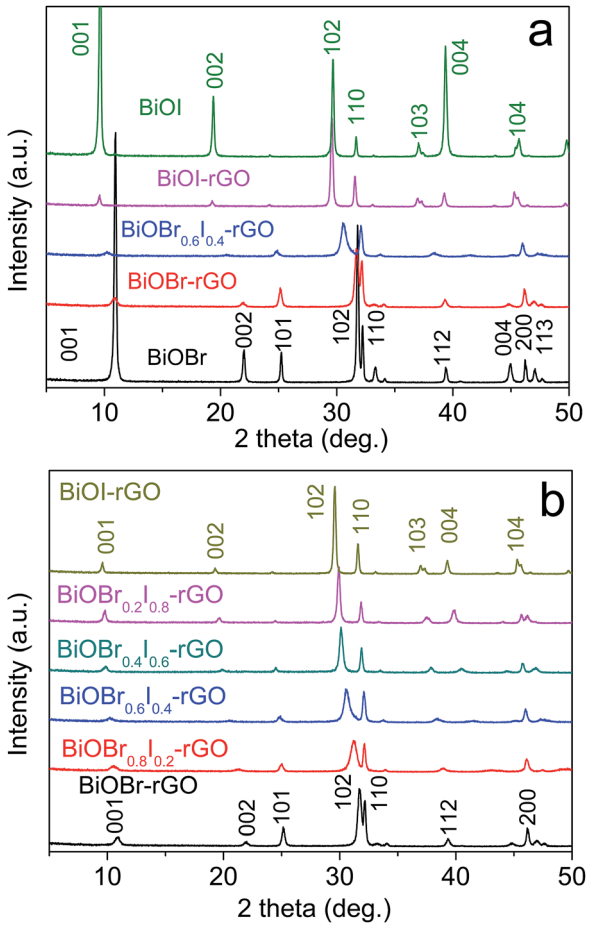

Fig. 1 XRD patterns of $BiOBr_xI_{1-x}$–rGO samples, as well as pure BiOBr and BiOI.

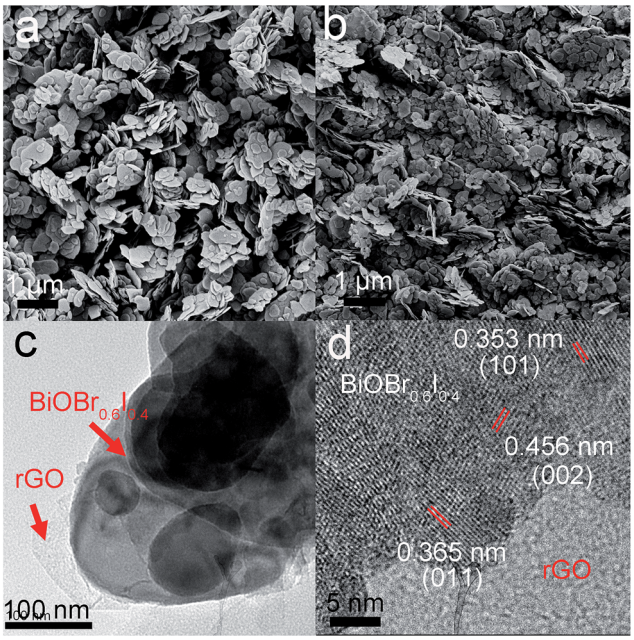

Fig. 2 SEM images of (a) $BiOBr_{0.6}I_{0.4}$, (b) $BiOBr_{0.6}I_{0.4}$–rGO samples; (c) TEM image, and (d) HR-TEM image of $BiOBr_{0.6}I_{0.4}$–rGO sample.

that the solid solution of $BiOBr_xI_{1-x}$ in $BiOBr_xI_{1-x}$–rGO composites depicted a medium interlayer spacing between pure BiOBr and BiOI. Moreover, the evolution of XRD pattern upon the variation for molar ratio of Br^-/I^- was shown in Fig. 1b. With increase of the content of I^- ion, the (001) diffraction gradually shifted from high angle of pure BiOBr to low angle of pure BiOI, which demonstrated the enlargement of interlayer spacing step by step. This result can be ascribed to the successful formation of solid solution of $BiOBr_xI_{1-x}$. In addition, no diffraction peaks for carbon species observed should result from the low amount (1.0 wt%) of reduced graphene oxide and its well dispersion in these composites. With respect to the existence of rGO, it was further proved by the below TEM and Raman spectra studies.

The morphology and structure of $BiOBr_xI_{1-x}$–rGO were examined by electronic microscopy technologies (Fig. 2). As shown in Fig. 2a, the $BiOBr_{0.6}I_{0.4}$ sample exhibited a lot of separate irregular nanoflakes with diameters of 0.2–0.5 μm. With the *in situ* growth on graphene, besides the diminishing of nanoflake thickness as illustrated by XRD results, the lateral size of nanoflakes was apparently decreased (Fig. 2b). Additionally, rGO was also unable to be observed in FE-SEM image due to its extremely thin thickness. Fig. 2c depicted the TEM image of $BiOBr_{0.6}I_{0.4}$–rGO composite. The flake-like aspect was similar to the morphology of $BiOBr_{0.6}I_{0.4}$ in FE-SEM image, and furthermore some exceedingly thin nanosheets covered on $BiOBr_{0.6}I_{0.4}$ flakes were checked, which should be assigned as rGO nanosheets. Fig. 2d exhibited the HRTEM image of $BiOBr_{0.6}I_{0.4}$–rGO composite, where three kinds of different lattice fringes images were found with spacing of 0.353 nm, 0.365 nm and 0.456 nm, respectively corresponding to (101), (011) and (002) planes of $BiOBr_{0.6}I_{0.4}$.

Raman spectroscopy technology is a powerful tool to characterize the electronic and structural properties of graphene and graphene-based materials in particular providing valuable information about disorder and defect carbon structures. Representative Raman peaks of graphene were presented in

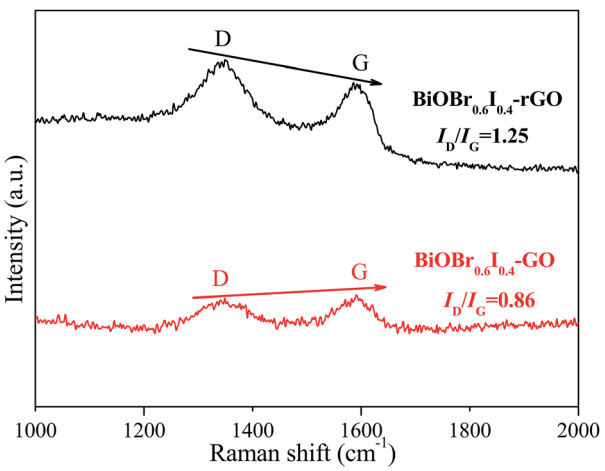

Fig. 3 Raman spectra of $BiOBr_{0.6}I_{0.4}$–rGO and $BiOBr_{0.6}I_{0.4}$–GO composites.

Fig. 3 for $BiOBr_{0.6}I_{0.4}$–rGO and $BiOBr_{0.6}I_{0.4}$–GO composites. The peaks at 1346 cm^{-1} (D band) and 1594 cm^{-1} (G band) were observed in the two composites, which were ascribed to the graphite structures. The intensity of D band (the symmetry A_{1g} mode) reflects the degree of edge chirality and the G band (the E_{2g} mode of sp^2 carbon atoms) represents the relative degree of graphitization. The intensity ratio of D band to G band (I_D/I_G) is proposed to an indication of disorder in GO or rGO, originating from defects associated with vacancies, grain boundaries, and amorphous carbons.[47] In comparison with $BiOBr_{0.6}I_{0.4}$–GO, the ratio of D/G intensity in $BiOBr_{0.6}I_{0.4}$–rGO increased significantly, which suggested the successful reduction of graphene oxide.

The optical property of $BiOBr_xI_{1-x}$–rGO, as well as pure BiOBr and BiOI was investigated by UV-vis diffused reflectance spectra (Fig. S1†). It was obvious that the absorption edges of BiOBr and BiOI were at approximately 422 nm and 657 nm, respectively, which were similar to the previous reports.[36] After combination with reduced graphene oxide, the absorption edges of BiOBr–rGO and BiOI–rGO had no apparent change, which suggested their band structures were not influenced in the *in situ* growth process. The composites of solid solutions with reduced graphene oxide showed a trend of gradual red-shift of absorption edge with the decrease of Br^-/I^-, which was similar to the variation of interlayer spacing from XRD examination. This result could be explained by the successful formation of solid solution. The band gap of these solid solutions in $BiOBr_xI_{1-x}$–rGO was studied by the following formula:

$$\alpha h\nu = A(h\nu - E_g)^{n/2} \quad (1)$$

where α, ν, E_g, and A are absorption coefficient, light frequency, band gap and a constant, respectively.[28–32] The n value is determined by the type of optical transition characteristics of a semiconductor ($n = 1$ for direct transition and $n = 4$ for indirect transition). According to previous studies, the value of n for BiOX is 4.[36] Therefore, the band-gap energy could be estimated from a plot of $(\alpha h\nu)^{1/2}$ *vs.* photon energy ($h\nu$) (Fig. 4), which were

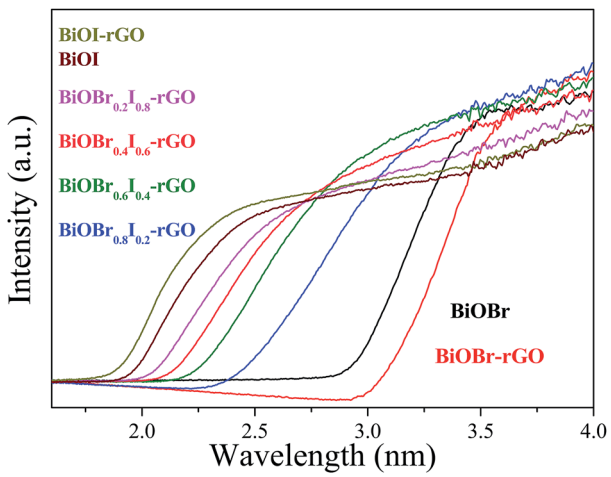

Fig. 4 Plots of $(\alpha h\nu)^{1/2}$ *vs.* photon energy ($h\nu$) of $BiOBr_xI_{1-x}$–rGO samples, as well as pure BiOBr and BiOI.

3.05, 2.41, 2.25, 2.13, 2.04 and 1.89 eV for BiOBr–rGO, $BiOBr_{0.8}I_{0.2}$–rGO, $BiOBr_{0.6}I_{0.4}$–rGO, $BiOBr_{0.4}I_{0.6}$–rGO, $BiOBr_{0.2}I_{0.8}$–rGO and BiOI–rGO, respectively.

Photocatalytic study of $BiOBr_xI_{1-x}$–rGO composites

The photocatalytic activities of $BiOBr_xI_{1-x}$–rGO samples were evaluated by the degradation of MO in an aqueous solution under visible light irradiation. Fig. 5a showed the change for absorption spectra of MO aqueous solution under visible light irradiation with the presence of $BiOBr_{0.6}I_{0.4}$–rGO composite. Obviously, the absorbance of MO at 464 nm decreased sharply and almost disappeared after 20 min. The result of chemical oxygen demanded (COD) examination (Fig. 5b) indicated that organic dyes have been completely degraded to small molecules, not only destroy the chromophoric groups. It is well known that there are three possible routes for MO photodegradation: photolysis, dye photosensitization and photocatalytic process. In order to confirm the degradation process, the blank experiment with the absence of photocatalyst and the photocatalytic test with Degussa P25 under visible light were also investigated. As illustrated in Fig. 5c, the MO photocatalysis was negligible, which indicated that MO molecules were extremely stable under visible light. The slight degradation of MO on P25 (Fig. 6a) also demonstrated the dye-sensitization was insignificant. Therefore, the rapid removal of dyes in these experiments mainly resulted from the photocatalytic effect.

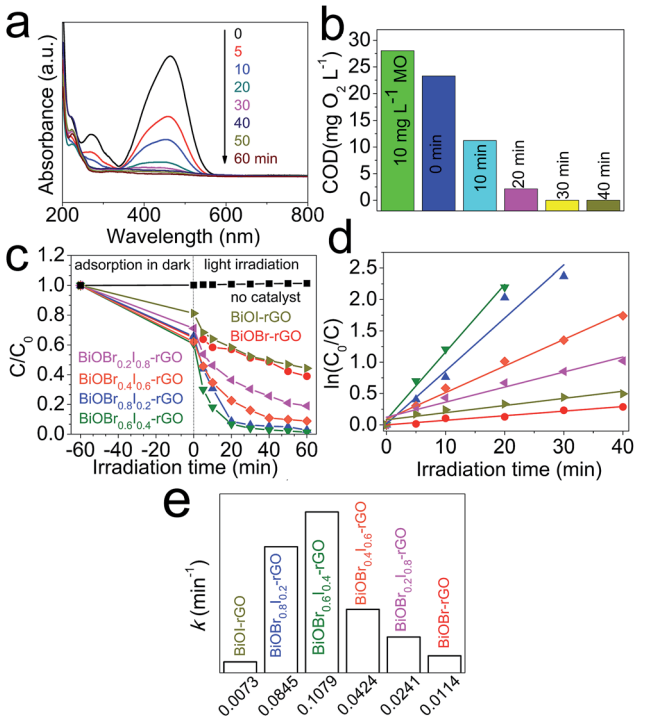

Fig. 5 (a) The real-time absorption spectra and (b) the COD value of MO solution with the presence of $BiOBr_{0.6}I_{0.4}$–rGO composite under visible light irradiation; (c) degradation ratios, (d) first-order kinetics data and (e) rate constants of the photocatalytic removal of MO by various $BiOBr_xI_{1-x}$–rGO photocatalysts under visible light irradiation.

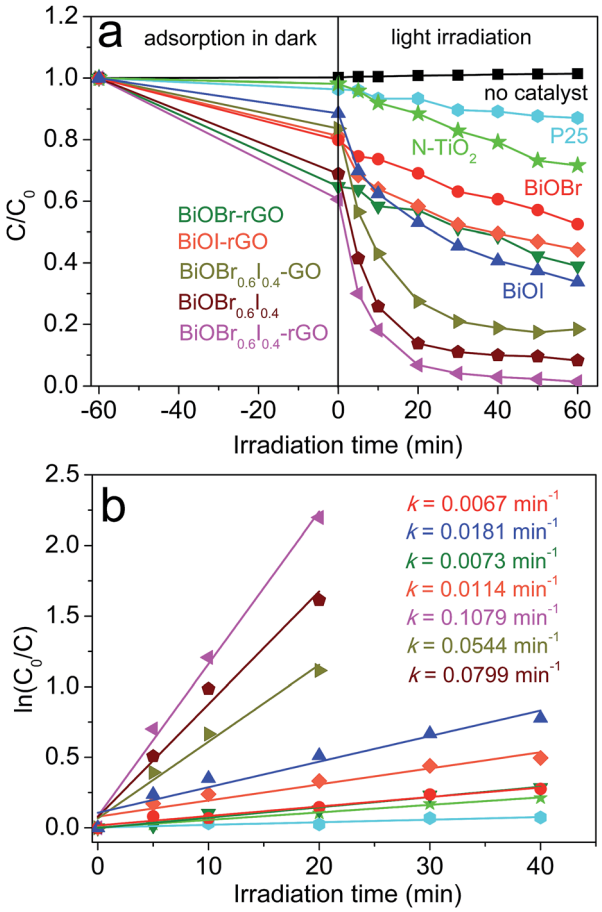

Fig. 6 (a) Degradation ratios and (b) first-order kinetics data of the photocatalytic removal of MO by different photocatalysts.

The influence of Br^-/I^- molar ratio on the photocatalytic activity of $BiOBr_xI_{1-x}$–rGO composites was investigated and the results were present in Fig. 5c. A relatively low activity was achieved on these composites of rGO with pure BiOBr and BiOI. Only 61.1% and 55.7% of MO were respectively decomposed on BiOBr–rGO and BiOI–rGO after irradiation for 60 min. It was clear that the $BiOBr_xI_{1-x}$–rGO samples displayed more excellent photocatalytic performance in comparison with BiOBr–rGO and BiOI–rGO. As the optimal photocatalyst, $BiOBr_{0.6}I_{0.4}$–rGO composite possessed the highest photocatalytic activity, and could remove 93.3% MO molecules within the initial 20 min. To quantitatively understand the reaction rate of MO degradation, the photocatalytic kinetic study was investigated by the pseudo-first order model with the following equation:

$$\ln(C_0/C) = kt \quad (2)$$

where C_0 and C are the concentrations of MO at time 0 (the time to obtain adsorption–desorption equilibrium) and t, respectively, and k is the pseudo-first-order rate constant (Fig. 5d). As see from Fig. 5e, the rate constants k of BiOBr–rGO, $BiOBr_{0.8}I_{0.2}$–rGO, $BiOBr_{0.6}I_{0.4}$–rGO, $BiOBr_{0.4}I_{0.6}$–rGO, $BiOBr_{0.2}I_{0.8}$–rGO and BiOI–rGO were respectively calculated to 0.0073, 0.0845, 0.1079, 0.0424, 0.0241 and 0.0014 min^{-1}. The optimum photocatalytic activity of $BiOBr_{0.6}I_{0.4}$–rGO composite for degradation of MO was almost 14.8 and 9.5 times as high as those of BiOBr–rGO and BiOI–rGO, respectively. The above results sufficiently certified the formation of $BiOBr_xI_{1-x}$–rGO composites could effectively enhance the photocatalytic performance.

For comparison, other photocatalysts of P25 TiO_2, N-modified TiO_2, BiOBr, BiOI, $BiOBr_{0.6}I_{0.4}$ and $BiOBr_{0.6}I_{0.4}$–GO were also prepared for the degradation of MO (Fig. 6a). As expected, the visible inactive photocatalyst of P25 displayed poor photocatalytic activity, and the visible active N-modified TiO_2 showed a 28.4% degradation ratio after 60 min irradiation. These individual BiOBr and BiOI also depicted low activity, and the performance was greatly improved by a solid solution of $BiOBr_{0.6}I_{0.4}$ because of the promoted light harvest and carrier separation, whereas, its activity was still much lower than that of $BiOBr_{0.6}I_{0.4}$–rGO. Moreover, for the weaker electric conductivity of graphene oxide than reduced graphene oxide, the composite of $BiOBr_{0.6}I_{0.4}$–GO illustrated an inferior photocatalytic performance in contrast with $BiOBr_{0.6}I_{0.4}$–rGO. As displayed in Fig. 6b, the rate constants for MO photodegradation by $BiOBr_{0.6}I_{0.4}$–rGO were 59.9, 20.4, 16.1, 6.0, 1.4 and 2.0 times than those of P25 (0.0018 min^{-1}), N-modified TiO_2 (0.0053 min^{-1}), BiOBr (0.0067 min^{-1}), BiOI (0.0181 min^{-1}), $BiOBr_{0.6}I_{0.4}$ (0.0799 min^{-1}) and $BiOBr_{0.6}I_{0.4}$–GO (0.0544 min^{-1}), respectively.

Besides the high activity, the stability of photocatalysts was also very important for practical application. Fig. S2† depicted the photocatalytic performance of $BiOBr_{0.6}I_{0.4}$–rGO for degradation of MO with six successive experiments. As we could see, the MO degradation efficiency only declined by 19.7% after six cycles, and we supposed that the mass loss in the progress of recovery was the main reason for the decrease in photocatalytic activity of reused photocatalyst in six repeated cycles.

Possible photocatalytic mechanism of $BiOBr_xI_{1-x}$–rGO composites

The above results revealed that the formation of $BiOBr_xI_{1-x}$–rGO composites could effectively enhance their photocatalytic performance under visible light irradiation. On the basic of experimental data, a possible photocatalytic mechanism of $BiOBr_{0.6}I_{0.4}$–rGO composite was explained as follows (Fig. 7). The valence band potentials (E_{VB}) of solid solution $BiOBr_{0.6}I_{0.4}$ was estimated according to the following equation of $E_{VB} = X - E_e + 0.5E_g$, where X and E_e were respective the electronegativity of semiconductor and the energy of free electrons on the hydrogen scale (about 4.50 eV). Thus, the conduct band edge potential (E_{CB}) could be determined by $E_{CB} = E_{VB} - E_g$. The conduction band (CB) and valence band (VB) edge potentials of $BiOBr_{0.6}I_{0.4}$ were estimated to be 0.46 eV and 2.71 eV. According to the p-type semiconductor nature of BiOX, the Fermi energy level (E_f) of $BiOBr_{0.6}I_{0.4}$ locates near the VB edge. Because of the much more negative position of rGO E_f level (−0.08 eV),[48–50] after coupling with rGO, electrons on rGO would transfer to $BiOBr_{0.6}I_{0.4}$ until to create a new balance. Driven by the internal electron field on the interface, the photoinduced electrons would transfer to rGO and leave holes on the VB of $BiOBr_xI_{1-x}$,

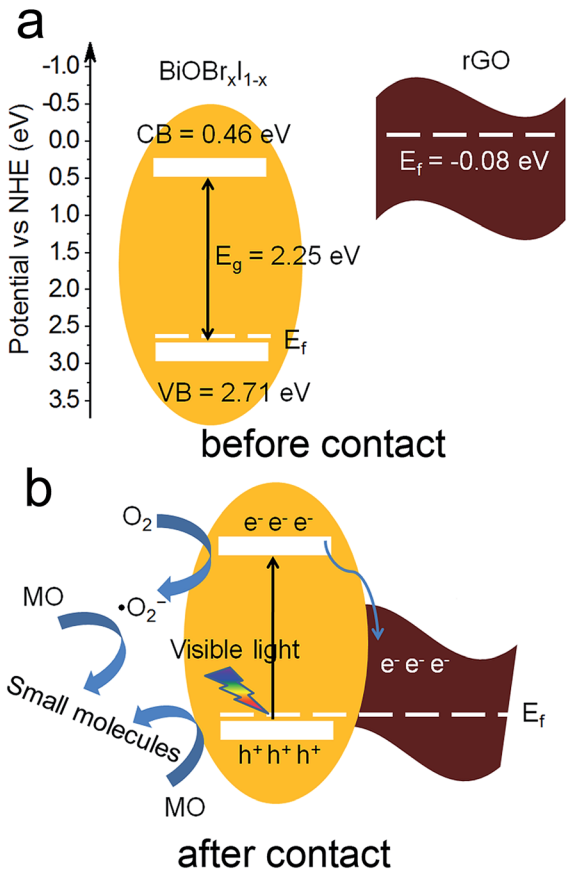

Fig. 7 Schematic diagram for (a) energy bands of $BiOBr_xI_{1-x}$ and Fermi level of rGO before contact; (b) the band structure of $BiOBr_xI_{1-x}$–rGO and its possible photocatalytic mechanism under visible-light irradiation.

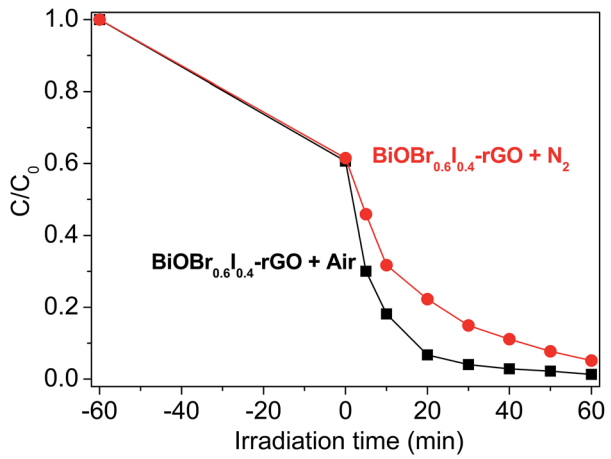

Fig. 8 The photodegradation performance of MO with the presence of $BiOBr_{0.6}I_{0.4}$–rGO under the air and N_2 atmosphere.

therefore suppressing the recombination of carriers. A reduced photoluminescence (PL) intensity of $BiOBr_xI_{1-x}$–rGO composite compared to individual $BiOBr_xI_{1-x}$ was illustrated in Fig. S3† that proved this efficient separation. Given the low concentration of rGO in composites, a portion of $BiOBr_{0.6}I_{0.4}$ surface was

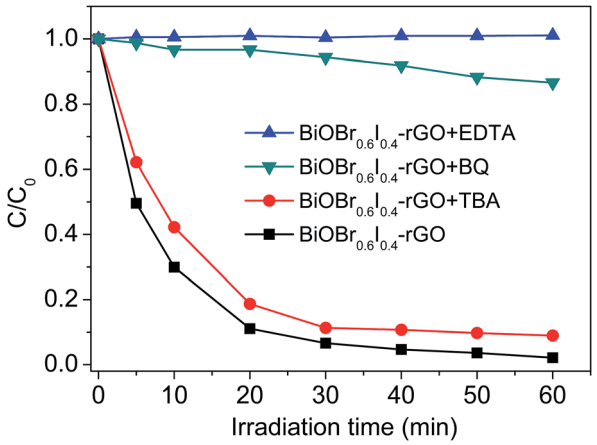

Fig. 9 Photocatalytic degradation of MO by $BiOBr_{0.6}I_{0.4}$–rGO photocatalyst with or without the addition of various quenchers.

not covered by rGO. Some electrons on CB of $BiOBr_{0.6}I_{0.4}$ would reduced the adsorbed O_2 to superoxide radical ($^{\bullet}O_2^-$) that is a common active species in photocatalysis process. The compared experiments in air or nitrogen atmosphere (Fig. 8) suggested that the presence of oxygen was beneficial to enhance photocatalytic performance.[51]

The $^{\bullet}OH$ is another active specie in the photocatalytic degradation. Theoretically, the holes on the surface of $BiOBr_xI_{1-x}$–rGO samples can oxidize H_2O to $^{\bullet}OH$ because the VB of $BiOBr_xI_{1-x}$–rGO composites are more positive than E^0 ($^{\bullet}OH/OH^-$) (2.38 eV). However, the generation of $^{\bullet}OH$ almost impossible due to the standard redox potential of Bi^V/Bi^{III} (1.59 eV) being more negative than that of $^{\bullet}OH/OH^-$(2.38 eV).[33] Therefore, we believe holes and $^{\bullet}O_2^-$ are two main active species during the photocatalytic reaction happened.

In order to verify the above speculation, we also used the trapping experiments to further determine the main active species of $BiOBr_{0.6}I_{0.4}$–rGO composite for the degradation of MO (Fig. 9). As shown in the figure, the MO degradation was significantly suppressed by adding benzoquinone (BQ, 0.5 mM, a quencher of $^{\bullet}O_2^-$) and disodium ethylenediaminetetraacetate (EDTA, 6 mM, a quencher of holes),[52–54] respectively. However, the degradation efficiency of MO was showed no obvious influence on photocatalyst by adding *tert*-butyl alcohol (TBA, 6 mM, a quencher of $^{\bullet}OH$). These results clearly demonstrated that $^{\bullet}O_2^-$ and h_{VB}^+ should be the main active species in $BiOBr_xI_{1-x}$–rGO composites system under visible light irradiation for the photocatalytic degradation of MO.

Conclusions

We have successfully synthesized a composite photocatalyst of $BiOBr_xI_{1-x}$–rGO that was obtained by controllable *in situ* growth of $BiOBr_xI_{1-x}$ solid solution on reduced graphene oxide. The optimal $BiOBr_{0.6}I_{0.4}$–rGO sample exhibited excellent photocatalytic activity in the degradation of MO under visible light irradiation. On the basis of characterization results, we attributed the enhanced photocatalytic activity to the more effective

electron–hole separation and transportation. Moreover, the photocatalyst depicted a great stability that the photodecomposition rate of MO could still retain over 80% after six cycles.

Acknowledgements

We gratefully acknowledge the financial support from the National Natural Science Foundation of China (51202288), the 521 talent project of ZSTU, the program of Graduate Innovation Research in ZSTU (YCX13001) and the project-sponsored by the Scientific Research Foundation (SRF) for the Returned Overseas Chinese Scholars (ROCS), State Education Ministry (SEM).

Notes and references

1 A. Fujishima and K. Honda, *Nature*, 1972, **238**, 37.
2 H. Tong, S. Ouyang, Y. Bi, N. Umezawa, M. Oshikiri and J. Ye, *Adv. Mater.*, 2012, **24**, 229.
3 X. Chen, S. Shen, L. Guo and S. S. Mao, *Chem. Rev.*, 2010, **110**, 6503.
4 K. Zhang, C. Liu, F. Huang, C. Zheng and W. Wang, *Appl. Catal., B*, 2006, **68**, 125.
5 Y. Huo, J. Zhang, M. Miao and Y. Jin, *Appl. Catal., B*, 2012, **111–112**, 334.
6 H. Liu, Y. Su, Z. Chen, Z. Jin and Y. Wang, *J. Hazard. Mater.*, 2014, **266**, 75.
7 J. Hu, S. Weng, Z. Zheng, Z. Pei, M. Huang and P. Liu, *J. Hazard. Mater.*, 2014, **264**, 293.
8 J. Xia, S. Yin, H. Li, H. Xu, Y. Yan and Q. Zhang, *Langmuir*, 2010, **27**, 1200.
9 D. Yue, D. Chen, Z. Wang, H. Ding, R. Zong and Y. Zhu, *Phys. Chem. Chem. Phys.*, 2014, **16**, 26314.
10 Y. Jiang, S. Chou, J. Chang, S. Huang, H. Lin and C. Chen, *RSC Adv.*, 2015, **5**, 30851.
11 S. Ge, K. Zhao and L. Zhang, *J. Nanopart. Res.*, 2012, **14**, 1015.
12 Z. Jia, F. Wang, F. Xin and B. Zhang, *Ind. Eng. Chem. Res.*, 2011, **50**, 6688.
13 J. Xiong, Q. Dong, T. Wang, Z. Jiao, G. Lu and Y. Bi, *RSC Adv.*, 2014, **4**, 583.
14 R. Hao, X. Xiao, X. Zuo, J. Nan and W. Zhang, *J. Hazard. Mater.*, 2012, **209**, 137.
15 J. Li, Y. Zhu, Y. Yan, B. Xi, K. Tang and Y. Qian, *J. Nanosci. Nanotechnol.*, 2012, **3**, 2068.
16 F. Tian, J. Xiong, H. Zhao, Y. Liu, S. Xiao and R. Chen, *CrystEngComm*, 2014, **16**, 4298.
17 M. Guerrero, A. Altube, E. Lecina, E. Rossinyol, M. Dolors, E. Pellicer and J. Sort, *ACS Appl. Mater. Interfaces*, 2014, **6**, 13994.
18 F. Duo, Y. Wang, X. Mao, C. Fan and H. Zhang, *Cryst. Res. Technol.*, 2014, **49**, 721.
19 J. Fu, Y. Tian, B. Chang, F. Xi and X. Dong, *J. Mater. Chem.*, 2012, **22**, 21159.
20 X. Wang, Q. Wang, F. Li, W. Yang, Y. Zhao, Y. Hao and S. Liu, *Chem. Eng. J.*, 2013, **234**, 361.
21 Y. Tian, B. Chang, Z. Yang, B. Zhou, F. Xi and X. Dong, *RSC Adv.*, 2014, **4**, 4187.
22 W. Xiong, Q. Zhao, X. Li and D. Zhang, *Catal. Commun.*, 2011, **16**, 229.
23 J. Di, J. Xia, Y. Ge, L. Xu, H. Xu, J. Chen, M. He and H. Li, *Dalton Trans.*, 2014, 15429.
24 Z. Cui, F. Zhang, Z. Zheng, W. Fa and B. Huang, *Mater. Technol.*, 2014, **29**, 214.
25 H. Jiao, X. Yu, Z. Liu, P. Kuang and Y. Zhang, *RSC Adv.*, 2015, **5**, 16239.
26 J. Xia, J. Di, S. Yin, H. Xu, J. Zhang, Y. Xu, L. Xu, H. Li and M. Ji, *RSC Adv.*, 2014, **4**, 82.
27 L. Kong, Z. Jiang, T. Xiao, L. Lu, M. Jones and P. Edwards, *Chem. Commun.*, 2011, **47**, 5512.
28 L. Lu, L. Kong and Z. Jiang, *Catal. Lett.*, 2012, **142**, 771.
29 Z. Liu, B. Wu, Y. Zhao, J. Niu and Y. Zhu, *Ceram. Int.*, 2014, **40**, 5597.
30 Z. Liu, B. Wu and Y. Zhu, *Catal. Lett.*, 2012, **142**, 1489.
31 R. Wang, G. Jiang, X. Wang, R. Hu, X. Xi, S. Bao, Y. Zhou, T. Tong, S. Wang, T. Wang and W. Chen, *Powder Technol.*, 2012, **228**, 258.
32 B. Parea, B. Sarwana and S. Jonnalagadda, *Appl. Surf. Sci.*, 2011, **258**, 247.
33 Z. Jia, F. Wang, F. Xin and B. Zhang, *Ind. Eng. Chem. Res.*, 2011, **50**, 6688.
34 Z. Xu, L. Han, B. Lou, X. Zhang and S. Dong, *J. Mater. Chem. C*, 2014, **2**, 2470.
35 X. Chang, M. Gondal, A. Al-Saadi, M. Ali, H. Shen, Q. Zhou, J. Zhang, M. Du, Y. Liu and G. Ji, *J. Colloid Interface Sci.*, 2012, **377**, 291.
36 J. Cao, B. Xu, B. Luo, H. Lin and S. Chen, *Catal. Commun.*, 2011, **13**, 63.
37 O. Compton and S. Nguyen, *Small*, 2010, **6**, 711.
38 F. Bonaccorso, A. Lombardo, T. Hasan, Z. Sun, L. Colombo and A. Ferrari, *Mater. Today*, 2012, **15**, 564.
39 A. Bianco, H. Cheng, T. Enoki, Y. Gogotsi and R. Hurt, *Carbon*, 2013, **65**, 1.
40 Q. Xiang, J. Yu and M. Jaroniec, *Chem. Soc. Rev.*, 2012, **41**, 782.
41 H. Zhu, P. Huang, L. Jing, T. Zuo, Y. Zhao and X. Gao, *J. Mater. Chem.*, 2012, **22**, 2063.
42 N. Zhang, Y. Zhang and Y. Xu, *Nanoscale*, 2012, **4**, 5792.
43 Z. H. Ai, W. K. Ho and S. C. Lee, *J. Phys. Chem. C*, 2011, **115**, 25330.
44 Z. Liu, W. C. Xu, J. Z. Fang, X. X. Xu, S. X. Wu, X. M. Zhu and Z. H. Chen, *Appl. Surf. Sci.*, 2012, **259**, 441.
45 H. Liu, W. Cao, Y. Su, Z. Chen and Y. Wang, *J. Colloid Interface Sci.*, 2013, **398**, 161.
46 L. Tian, J. Liu, C. Gong, L. Ye and L. Zan, *J. Nanopart. Res.*, 2013, **15**, 1917.
47 Z. Liu, W. Xu, J. Fang, X. Xu, S. Wu, X. Zhu and Z. Chen, *Appl. Surf. Sci.*, 2012, **259**, 441.
48 M. Zhu, Y. Dong, B. Xiao, Y. Du, P. Yang and X. Wang, *J. Mater. Chem.*, 2012, **22**, 23773.
49 H. Park, E. Bae, J. Lee, J. Park and W. Choi, *J. Phys. Chem. B*, 2006, **110**, 8740.
50 Z. Xiong, L. Zhang, J. Ma and X. Zhao, *Chem. Commun.*, 2010, **46**, 6099.

51 J. Li, X. Jiang, L. Lin, J. Zhou, G. Xu and Y. Yuan, *J. Mol. Catal. A: Chem.*, 2015, **406**, 46.
52 M. Elovitz and U. Gunten, *Ozone: Sci. Eng.*, 1999, **21**, 239.
53 X. Li, N. Kikugawa and J. Ye, *Adv. Mater.*, 2008, **20**, 3816.
54 Y. Zhang, N. Zhang, Z. Tang and Y. Xu, *Chem. Sci.*, 2013, **4**, 1820.